Integration of Self-Assembled Epitaxial $BiFeO_3$–$CoFe_2O_4$ Multiferroic Nanocomposites on Silicon Substrates

*Dong Hun Kim, Nicolas M. Aimon, Xue Yin Sun, Lior Kornblum, Fred. J. Walker, Charles. H. Ahn, and Caroline A. Ross**

Perovskite-spinel epitaxial nanocomposite thin films are commonly grown on single crystal perovskite substrates, but integration onto a Si substrate can greatly increase their usefulness in devices. Epitaxial $BiFeO_3$–$CoFe_2O_4$ nanocomposites consisting of $CoFe_2O_4$ pillars in a $BiFeO_3$ matrix are grown on (001) Si with two types of buffer layers: molecular beam epitaxy (MBE)-grown $SrTiO_3$-coated Si and pulsed-laser-deposited (PLD) $Sr(Ti_{0.65}Fe_{0.35})O_3$/$CeO_2$/yttria-stabilized ZrO_2/Si. The nanocomposite grows with the same crystallographic orientation and morphology as that observed on single crystal $SrTiO_3$ when the buffered Si substrates are smooth, but roughness of the $Sr(Ti_{0.65}Fe_{0.35})O_3$ promoted additional $CoFe_2O_4$ pillar orientations with 45° rotation. The nanocomposites on MBE-buffered Si show very high magnetic anisotropy resulting from magnetoelastic effects, whereas the hysteresis of nanocomposites on PLD-buffered Si can be understood as a combination of the hysteresis of the $Sr(Ti_{0.65}Fe_{0.35})O_3$ film and the $CoFe_2O_4$ pillars.

1. Introduction

Self-assembled nanocomposite thin films such as $BaTiO_3$-$CoFe_2O_4$ (BTO-CFO), $BiFeO_3$-$CoFe_2O_4$ (BFO-CFO), and $BiFeO_3$-$NiFe_2O_4$ (BFO-NFO), in which a ferrimagnetic spinel phase grows epitaxially as pillars within an immiscible ferroelectric perovskite phase, have been studied intensively as two-phase multiferroic materials.[1–4] In the perovskite-spinel system, coupling between the piezoelectric and magnetostrictive phases at the vertical interfaces can lead to magnetoelectric behavior at room temperature. However, vertical epitaxial nanocomposites have been almost exclusively grown on single crystal oxide substrates which limits their utility in microelectronic devices. Integration of nanocomposites on a Si platform would provide a path towards large scale and low cost devices such as multiferroic memory and logic.[5]

The epitaxial growth of perovskite films directly on a Si substrate is usually limited by the formation of an interface layer of amorphous silica. To circumvent this, buffer layers can be employed such as an epitaxial bilayer of CeO_2 on yttrium-stabilized zirconia (YSZ), upon which perovksite thin films have been grown such as $(La,Sr)CoO_3$, $BiFeO_3$, $Pb(Zr,Ti)O_3$, and $LaNiO_3$.[6–9] However, to avoid the growth of the spinel CFO (111) orientation which occurs on YSZ- or CeO_2/YSZ-buffered Si (001),[10,11] a three layer buffer consisting of perovskite/CeO_2/YSZ-buffered Si (001) is proposed. This stack is expected to be an appropriate substrate for growth of spinel/perovskite vertical nanocomposites with the same crystal orientation as nanocomposites on single crystal perovskite substrates. An alternative to using a relatively thick bilayer or trilayer buffer is to grow a perovskite layer directly on Si, upon which the nanocomposite could be grown. Recent advances in oxide molecular beam epitaxy has enabled thin $SrTiO_3$ (STO) to be grown on Si with high quality,[12,13] avoiding the need for thick buffer layers.

Growth of BTO-CFO or BTO-NFO vertical nanocomposites on trilayer buffer layers consisting of $MgIn_2O_4$/CeO_2/YSZ/Si or $(La,Sr)CoO_3$/CeO_2/YSZ/Si has been reported,[14,15] though a clear columnar nanocomposite structure was not reported in those examples. More recently, the growth of ZnO-$La_{0.7}Sr_{0.3}MnO_3$ wurtzite-perovskite and CeO_2-BTO fluorite-perovskite vertical nanocomposites was reported on a Si substrate using a ~100 nm thick TiN/$SrTiO_3$ bilayer buffer layer.[16,17] The magnetoresistance of the $La_{0.7}Sr_{0.3}MnO_3$-ZnO/$SrTiO_3$/TiN/Si and the ferroelectricity of CeO_2-BTO/$SrTiO_3$/TiN/Si matched that of similar films grown on single crystal STO.

Here we report on the microstructure and magnetic properties of BFO-CFO nanocomposites on both $Sr(Ti_{1-x}Fe_x)O_3$/CeO_2/YSZ/Si and STO/Si. We have found previously that $Sr(Ti_{1-x}Fe_x)O_3$ (STF) perovskite films can be grown epitaxially on CeO_2/YSZ-buffered (001) Si.[18–20] The STF grew as a single crystal (001)-oriented film, or exhibited both (001) and (011) 'double epitaxial' growth, depending on thickness and deposition conditions.[21] STF films grown in vacuum with x = 0.1~0.5 exhibited room-temperature magnetism and a strong out-of-plane anisotropy of magnetoelastic origin.[18–20] Therefore, as well as acting as a substrate for a vertical nanocomposite, the magnetism of

Dr. D. H. Kim, Dr. N. M. Aimon,
Dr. X. Y. Sun, Prof. C. A. Ross
Department of Materials Science and Engineering
Massachusetts Institute of Technology
Cambridge, Massachusetts 02139, USA
E-mail: caross@mit.edu
Dr. X. Y. Sun
School of Materials Science and Engineering
Harbin Institute of Technology
Harbin 150001, PR China
Dr. L. Kornblum, Dr. F. J. Walker, Prof. C. H. Ahn
Department of Applied Physics
Yale University
New Haven, CT 06520, USA

DOI: 10.1002/adfm.201401458

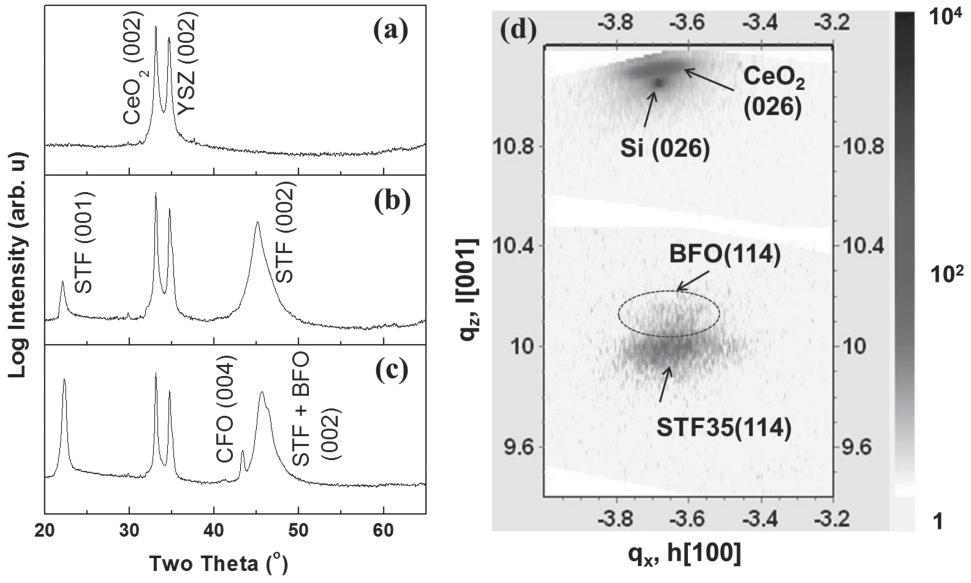

Figure 1. θ–2θ scans of (a) CeO_2/YSZ film on Si substrate, (b) STF35 thin film on CeO_2/YSZ/Si, and (c) BFO-CFO nanocomposite on STF35/CeO_2/YSZ/Si. (d) X-ray diffraction reciprocal space maps of BFO-CFO on STF35/CeO_2/YSZ/Si around the (026) reflection of Si.

the STF layer could influence the magnetic behavior of the nanocomposite. In addition to the STF/CeO_2/YSZ-buffered (001) Si, we also explored substrates in which the buffer layer consisted of a 20 unit cell thickness film of $SrTiO_3$, 8 nm thick, grown by molecular beam epitaxy (MBE) onto a Si (001) substrate from which the native oxide had been removed.

2. Results and Discussion

We first discuss the microstructure of the nanocomposites on STF35/CeO_2/YSZ/Si. **Figure 1**(a), (b), and (c) show X-ray diffraction (XRD) scans of CeO_2/YSZ/Si, STF35/CeO_2/YSZ/Si, and BFO-CFO nanocomposite on STF35/CeO_2/YSZ/Si, respectively. CeO_2/YSZ bilayers on Si showed only two peaks around $2\theta = 33.16°$ and 34.74° corresponding to CeO_2 (002) and YSZ (002) without any secondary phases. The STF35 on the CeO_2 also showed a single orientation with a (002) peak visible. The out-of-plane lattice parameter of STF35 was $c_{STF} = 4.016 \pm 0.003$ Å. The peak around 45° from the BFO-CFO nanocomposite on STF35 in Figure 1 (c) consisted of two overlapping peaks from BFO and STF35. BFO by itself did not grow well on buffered Si, so its lattice parameter could not be obtained from measurement of a homogeneous BFO film. However, we assign the lower angle peak to BFO because the unit cell volume of BFO grown at 5 mTorr on STO is bigger than that of STF35 deposited in vacuum on STO.[20,22] The STF35 peak shifted to higher angle compared to Figure 1(b) because the STF35, originally grown in vacuum, was exposed to a high temperature and 5 mTorr oxygen environment before and during the growth of the BFO-CFO, leading to a reduction in vacancy concentration and lattice parameter.

Figure 1(d) shows reciprocal space mapping (RSM) of the BFO-CFO nanocomposite on STF35/CeO_2/YSZ/Si around the asymmetric Si (026) peak. Mapping data were merged after scanning different ranges. The most intense Si peak yielded 5.431 ± 0.002 Å and 5.431 ± 0.003 Å as the in-plane and out-of-plane lattice parameters, the same as bulk Si (5.431 Å). The alignment of the CeO_2 (026) peak with the Si peak indicates that the ceria was coherently strained to the substrate with in-plane and out-of-plane lattice parameters of 5.432 ± 0.003 and 5.402 ± 0.006 Å respectively. A YSZ peak was not observed in this range of angles. The in-plane and out-of-plane lattice parameters calculated from the asymmetric STF35 (114) peak were respectively $a_{STF} = 3.875 \pm 0.010$ and $c_{STF} = 3.974 \pm 0.004$ Å. The unit cell volume was 59.672 $Å^3$ and the c/a ratio was 1.03 indicating a tetragonal distortion with in-plane compression. However, the STF35 was not fully oxidized during the process, because its unit cell volume was still larger than that of films of similar composition deposited in 5 mTorr oxygen on buffered Si, which were 58.66 $Å^3$ for STF34 and 58.73 $Å^3$ for STF36,[18] similar to bulk unit cell volumes predicted by Vegard's law of 58.77 and 58.73 $Å^3$ respectively.

In the nanocomposite, the BFO matrix was under tensile strain along the out-of-plane direction ($a_{BFO} = 3.923 \pm 0.013$ and $c_{BFO} = 4.006 \pm 0.006$ Å). The spinel CFO (228) peak was too weak to observe, but the out-of-plane lattice parameter from one dimensional XRD was $c_{CFO} = 8.347 \pm 0.002$ Å, showing that the CFO pillars were under compressive out-of-plane strain ($a_{CFO,bulk} = 8.390$ Å). We will show later that this strain state governs the magnetic properties of the nanocomposite.

Figure S1 shows φ scans of the BFO-CFO/STF35/CeO_2/YSZ/Si thin film indicating that each layer grew epitaxially with four-fold symmetry. The four-fold symmetrical epitaxial growth of perovskite and spinel nanocomposite thin films on (001) STO substrates has been reported by many groups.[24–26] Figure S2(a) illustrates the epitaxial relationship between BFO, STF35 and fluorite-structure CeO_2 and Figure S2(b) shows the cube-on-cube epitaxial growth of CFO on the STF35 layer. Considering the in-plane lattice parameters of bulk CFO and

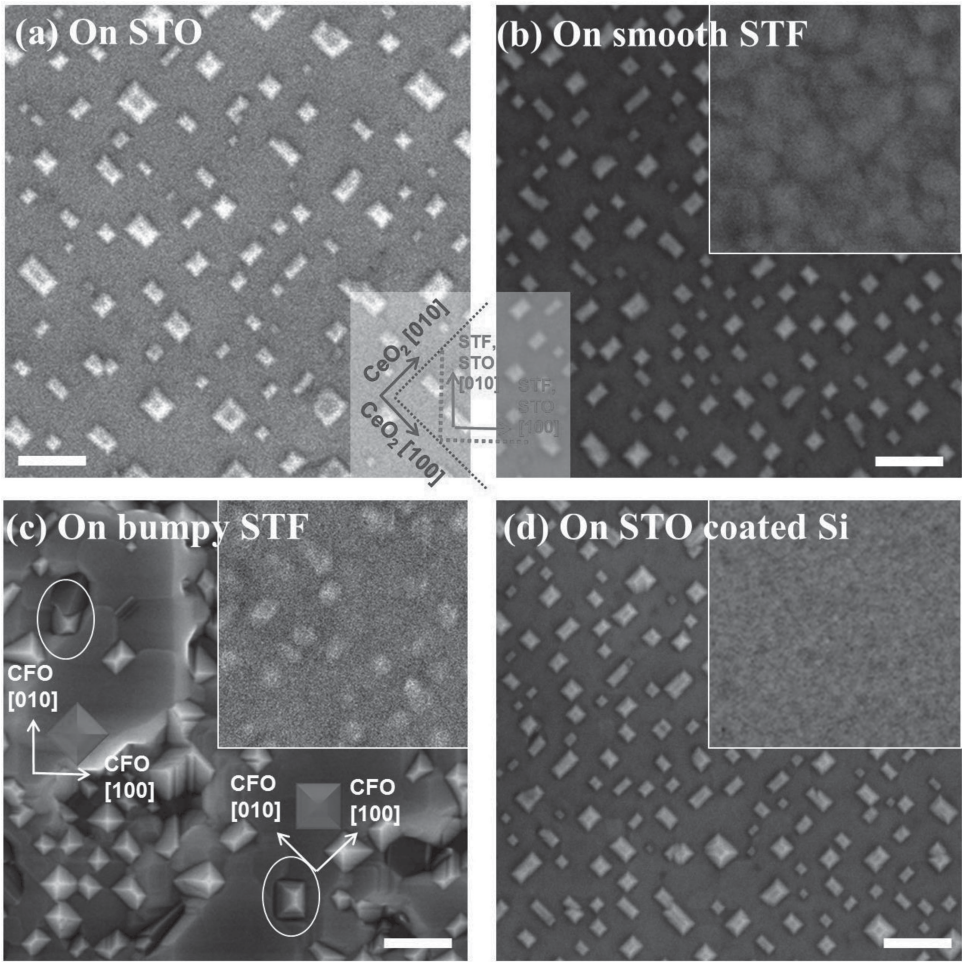

Figure 2. Top view SEM image of nanocomposite on (a) single crystal STO substrate, (b) smooth STF35/CeO_2/YSZ/Si, (c) rough STF35/CeO_2/YSZ/Si, and (d) STO/Si substrates. Scale bars correspond to 100 nm. Insets in (b), (c) and (d) are top view SEM images of STF35 and STO films before nanocomposite deposition at the same scale. The smooth STF35 film in inset of (b) was grown at 650 °C while the rough STF35 film was grown at 680 °C (inset in (c)). The circled CFO pillars in Figure 2 (a) are 45° rotated cube-on-cube epitaxial growth on STF35. The schematic diagram of cube-on-cube and 45° rotated cube-on-cube epitaxial growth are shown in (c).

STF35, an in-plane compressive strain would be expected in a continuous film of CFO on STF35. However, in the nanocomposite, the strain state in the CFO pillars is dominated by the *vertical* interfaces with the BFO, which explains the out-of-plane compression in the CFO pillars.

The θ-2θ and φ scans of the MBE grown STO layer on Si and the BFO-CFO/STO/Si are given in Figure S3. The 8 nm STO layer showed a (002) peak with out-of-plane lattice parameter of 3.928 ± 0.002 Å. In the nanocomposite, the φ scan indicates the expected 45° rotation between the (h0h) lattice planes of CFO and BFO vs. the Si substrate.

Figure 2 shows top view scanning electron microscope (SEM) images of BFO-CFO composites (a) on a single crystal STO substrate, (b) and (c) on STF35/CeO_2/YSZ-buffered Si substrates with different surface roughness, and (d) on the MBE STO-buffered Si substrate. Insets in Figure 2(b), (c), and (d) illustrate the surface morphology of the STF35 and STO layers before nanocomposite deposition. The nanocomposites on the STO substrate and on the STF layers were all grown at 630 °C while the nanocomposite on STO/Si was grown at 600 °C. The figures are oriented such that the BFO matrix in each sample has the same crystal directions. The [110] and [$\bar{1}$10] directions of CeO_2 are identifiable because they are parallel to the cleaving directions of the Si.

The BFO-CFO composites on STO, smooth STF35/CeO_2/YSZ/Si and STO/Si (Figures 2(a), (b) and (d) respectively) all show very similar plan-view morphologies in which square or rectangular CFO pillars are visible with parallel sides of length ~10–40 nm. The tops of the CFO nanopillars exhibited four tilted trapezoidal facets and one rectangular facet parallel to the plane, though the latter are small or absent in the sample of Figure 2(c). The four tilted facets correspond to CFO (111) which has the lowest surface energy, and the top plane corresponds to (001).[24,25] The vertical interfaces of the pillars represent {110} planes of BFO and CFO.

However, the rough STF35/CeO_2/YSZ/Si substrate produced a nanocomposite in which a minority of pillars exhibited a 45° rotation (Figure 2(c)). Further analysis of the pillar growth mode is shown in **Figure 3**. The transmission electron microscope (TEM) sample was cut parallel to the Si [100] axis, so the

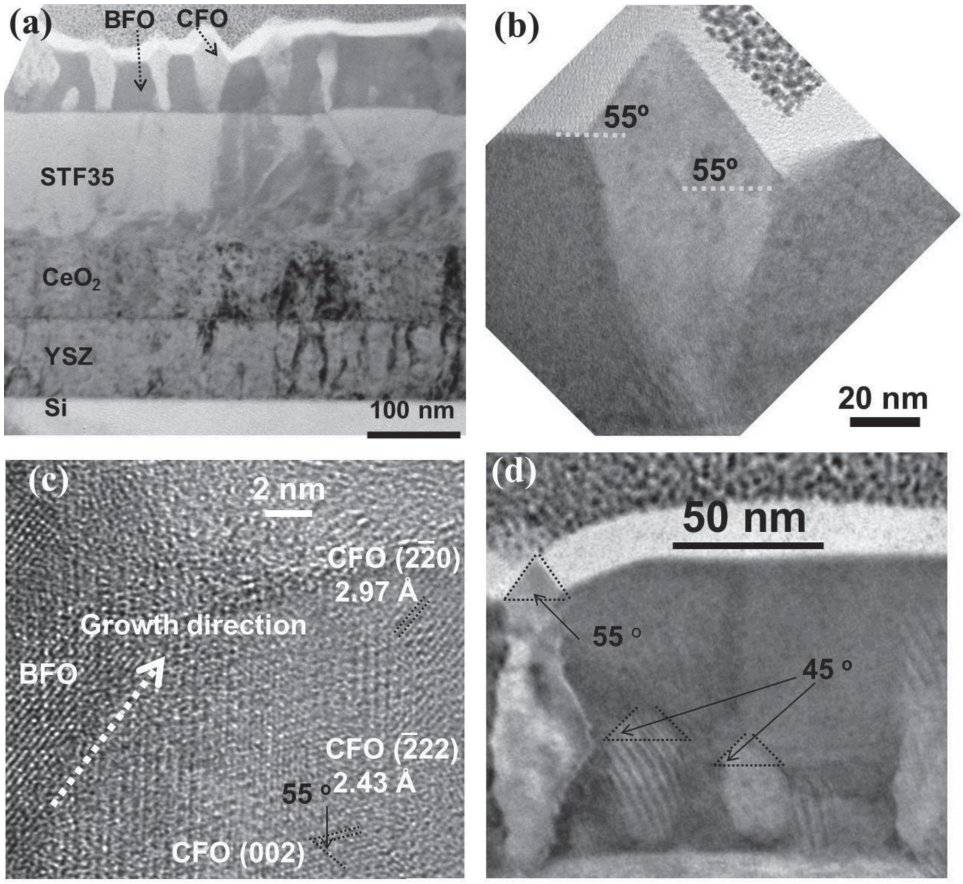

Figure 3. (a) Low magnification cross sectional TEM image of BFO-CFO nanocomposite grown on STF35/CeO_2/YSZ/Si. (b) Magnified cross sectional TEM image of a CFO pillar in BFO matrix on STF35/CeO_2/YSZ/Si after cutting by FIB, imaged along [110] of BFO. (c) HRTEM image of BFO-CFO interface. (d) CFO pillars in BFO matrix showing some pillars were overgrown by BFO.

direction normal to the sample plane is [110] of STF35 and BFO. Figure 3(a) is a low magnification cross sectional TEM image of the BFO-CFO nanocomposite thin film on the rough STF35/CeO_2/YSZ/Si showing sequential growth of buffer layers and clear separation of perovsite and spinel phases.

A magnified cross sectional TEM image of a majority-orientation CFO pillar (Figure 3(b)) shows an angle of 55° between the [001] surface of the BFO and the pillar facet. This is consistent with the facet plane of CFO being (111) and the image a projection parallel to a (101) plane of CFO, i.e. the (101) vertical facets of the CFO pillar were parallel to the [110] of BFO. Figure 3(c) is a high resolution TEM image around the BFO/CFO interface. The projection along [110] of BFO is also along the [110] direction of CFO for the majority pillars. Lattice images from ($\bar{2}22$) planes and from ($2\bar{2}0$) planes, which make an angle of 55° with (002) planes, can be seen. These observations are all consistent with the pillar having the usual crystal orientation seen in nanocomposites grown on smooth STO.

However, the TEM also revealed examples of the minority 45°-rotated pillars. In Figure 3(d) the two smaller pillars which were overgrown with BFO showed an angle of 45° between the projections of the vertical interface and the tilted top facet. This is consistent with a projection down a [100] direction of CFO, in which the vertical edge of the pillar and the edge between two top (111) facets are seen. This image, and others, suggest that some of the minority pillars grow more slowly and become covered by BFO, so only a fraction of them are observed in plan view images. The roughness of the substrate presumably provides more sites for CFO nucleation, especially if facets are present other than the (100) facet which the CFO does not wet well, and promotes the formation of CFO nuclei with different orientation. Indeed, small pits etched into an otherwise smooth STO substrate can be used as preferential nucleation sites for CFO pillars.[27] Additional nanocomposites grown on rough STF films are shown in Figure S4, illustrating a range of other pillar orientations.

Removing the BFO with an etchant allows the CFO pillars to be imaged directly, as well as relieving strain in the CFO. HCl is a good selective etchant for BFO which does not etch CFO, STO, STF35, CeO_2 and YSZ. An example is shown in **Figure 4**(a) which is a 45° tilted SEM image after 60 sec HCl etching of a sample grown on rough STF35.

The change in strain state caused by removing the BFO can be seen from XRD in Figure 4(c), from a sample grown on rough STF35. Etching led to the disappearance of BFO peaks while the STF35 peak remained. This supports the interpretation of overlapping STF35 (002) and BFO (002) peaks around $2\theta = 45°$ in Figure 1(c). The BFO removal also caused

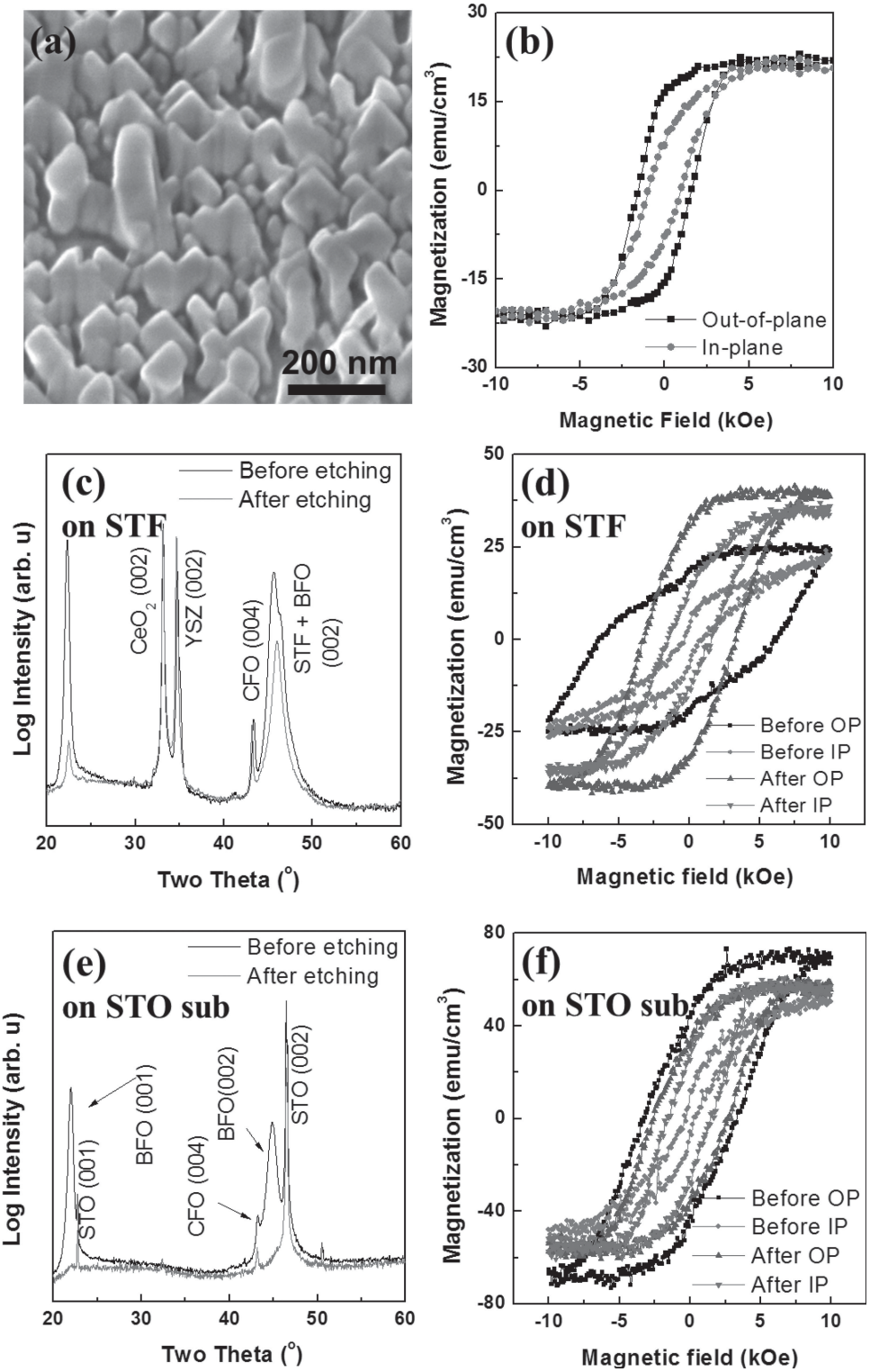

Figure 4. (a) 45° tilted SEM image of BFO-CFO nanocomposite on STF35/CeO_2/YSZ/Si substrate after etching in dilute HCl solution for 120 seconds at room temperature. (b) In-plane and out-of-plane magnetic hysteresis loops of STF35 thin film deposited at 680 °C and high vacuum (2×10^{-6} Torr) on buffered Si. XRD patterns of as deposited BFO-CFO nanocomposite on (c) STF35/CeO_2/YSZ/Si, (e) STO substrates. XRD patterns after HCl etching are overlaid. Magnetic hysteresis loops of BFO-CFO (d) on STF35/CeO_2/YSZ/Si, (f) on STO substrate before and after etching to remove BFO.

a peak shift of the CFO toward lower angle (shown in detail in Figure S5(a)) implying an out-of-plane lattice parameter increase. This was a result of the relaxation of the out-of-plane compressive strain imposed by the BFO. The out-of-lattice parameter of CFO relaxed from 8.347 ± 0.002 Å to 8.380 ± 0.002 Å which is close to the bulk value for CFO.

Figure 4(e) similarly compares the XRD pattern of BFO-CFO on single crystalline STO (001) substrates before and after etching. The CFO peak shifted to a lower angle but the degree of strain relaxation in the CFO on STF35 coated Si and STO substrates was significantly different. Strain relaxation has previously been observed after removing the BFO surrounding $MgFe_2O_4$ (MFO)[28] and CFO[29] pillars, but a report on CFO-BFO on a STO (001) substrate showed no such effect.[30] Our results unambiguously show strain relaxation in CFO by removing the BFO, and this has important effects on the magnetic properties which will be described next.

To understand the magnetic properties of the nanocomposites grown on STF35/CeO_2/YSZ/Si, we first need to describe the contribution of the STF35 layer. Figure 4(b) shows the room temperature measured in-plane and out-of-plane magnetic hysteresis loops of STF35/CeO_2/YSZ/Si. The STF35 film showed an out-of-plane easy axis in agreement with prior work on STF deposited on STO (001), $LaAlO_3$ (001), and CeO_2/YSZ buffered Si substrate due to its positive magnetostriction constant and out-of-plane tensile strain.[18–20] The saturation moment was 21.9 emu/cm^3 and the anisotropy field required to saturate the sample along a hard (in plane) axis was 6000 ± 200 Oe. The out-of-plane lattice parameter (4.016 Å) and saturation magnetic moment were similar those of STF35 grown on STO substrate.[20]

Figure 4(d) shows the magnetic hysteresis loops of the BFO-CFO nanocomposite on STF35 thin films. The magnetization was calculated for the whole film without normalizing to the volume fraction of spinel phases because it is difficult to estimate the volume fraction of spinel phase due to partial coverage by the BFO phase. The unetched BFO-CFO nanocomposite showed a hard magnetic behavior and could not be saturated at the maximum magnetic field attainable by the VSM of 10 kOe, so the hysteresis loops are in fact minor loops. The kink in the out-of-plane loop is attributed to the STF35 layer, showing that the STF35 was therefore still magnetic even though it had been partly oxidized during the growth of the BFO-CFO in 5 mTorr of oxygen.

The hysteresis loops of etched BFO-CFO nanocomposites on STF35/CeO_2/YSZ/Si and STO substrates are shown in Figure 4(d), and (f) respectively. For the sample on STF35/CeO_2/YSZ/Si, the out-of-plane anisotropy decreased dramatically on etching as the CFO strain relaxed, and the sample could be saturated at 10 kOe, explaining its apparently higher magnetic moment compared to the unetched sample. Samples with rough and smooth STF35 showed similar hysteresis. The sample on STO showed a smaller change.

The out-of-plane anisotropy is a result of both shape and magnetoelastic anisotropies. For example, a pillar aspect ratio of 3:1 would give a shape anisotropy of 1.9 kOe, based on a rod shaped pillar. Assuming that pillar shape and size are the same after etching, the change in anisotropy is a result of strain relaxation. The magnetoelastic anisotropy (H_{me}) was estimated as $H_{me} = \frac{3\lambda_{001} Y \varepsilon_{001}}{M_s}$ where λ_{001} is the magnetostriction coefficient (-350×10^{-6}),[31] Y is Young's modulus (141.6 GPa), ε_{001} is the compressive strain along the vertical direction, and M_s is the saturation magnetization (400 emu/cm^3).[32]

For the sample on STF35/CeO_2/YSZ/Si the compressive strain along the vertical direction changed from −0.0052 to −0.0012 on etching. The estimated magnetoelastic anisotropy field is then 19.3 kOe for the unetched and 4.5 kOe for the etched sample. In the case of the nanocomposite on single crystal STO, the strain relaxed from −0.0022 to −0.0011 respectively giving an estimated magnetoelastic anisotropy field of 8.2 kOe for the unetched and 4.1 kOe for the etched samples. The lower anisotropy measured for the sample on STO compared to that on STF35-coated Si, and the smaller change in its hysteresis loops on etching, are consistent with a dominant magnetoelastic anisotropy in the CFO-BFO nanocomposite system.

Finally, we show that the nanocomposites on MBE-buffered Si exhibited very high magnetic anisotropy resulting from magnetoelastic effects. **Figure 5**(a) shows a low magnification cross sectional TEM image of BFO-CFO/STO/Si after FIB cutting along the [100] direction of the CFO pillars, demonstrating clear phase separation in the nanocomposite. The CFO pillars in the nanocomposite on STO/Si showed an even higher out-of-plane compressive strain and magnetic anisotropy, Figure 4(b) and (c), than samples on STO or STF35. After HCl etching the BFO peak disappeared and the CFO peak shifted toward a lower angle, similar to nanocomposites on STF35/CeO_2/YSZ/Si and STO substrates, while the STO peak remained implying that the HCl removed only the BFO phase. The CFO peak shift after etching was bigger than that of composites on other substrates (Figure S5(c)). Table S1 gives the corresponding data for out-of-plane lattice parameters of BFO and CFO for both etched and unetched cases.

The out-of-plane loop of the unetched sample was far from saturation at 12.5 kOe, reaching only about 1/6 of its saturation moment at this field. The in-plane loop was a hard axis without hysteresis. This may be compared with the nanocomposite on STO substrate, Figure 4(f), which also had an out-of-plane easy axis with a coercivity of ~4 kOe. In Figure 5(d), out-of-plane magnetic hysteresis loops measured by SQUID and VSM at room temperature are compared at the same scale. The SQUID was able to saturate the CFO at about 24 kOe giving a coercivity of 12–13 kOe. The nanocomposite on STO/Si also showed a very large anisotropy change after HCl etching due to strain relaxation in the CFO. The out-of-plane compressive strain changed from −0.0067 to −0.0008 on etching and the estimated magnetoelastic anisotropy field was 25.0 kOe for the unetched and 3.0 kOe for the etched sample.

3. Conclusions

Perovskite-spinel BFO-CFO vertical nanocomposites were integrated on Si using two different buffered substrates: STF35/CeO_2/YSZ/Si and 8 nm STO/Si. For STO/Si and smooth STF35/CeO_2/YSZ/Si substrates, the nanocomposite adopted the same morphology and crystal orientation as is commonly found on STO. The BFO and CFO grew with a cube-on-cube epitaxy with BFO [100] ∥ STF or STO [100] and CFO [100] ∥ STF or STO [100], and the pillar sizes were similar between the samples. However, for rough STF35/CeO_2/YSZ/Si, other CFO orientations were also seen, in particular pillars with a 45° rotated growth with CFO [110] ∥ STF [100], attributed to nucleation of CFO with various orientations on the rough surface.

The nanocomposites showed a strong out-of-plane magnetic anisotropy as a result of both shape and magnetoelastic

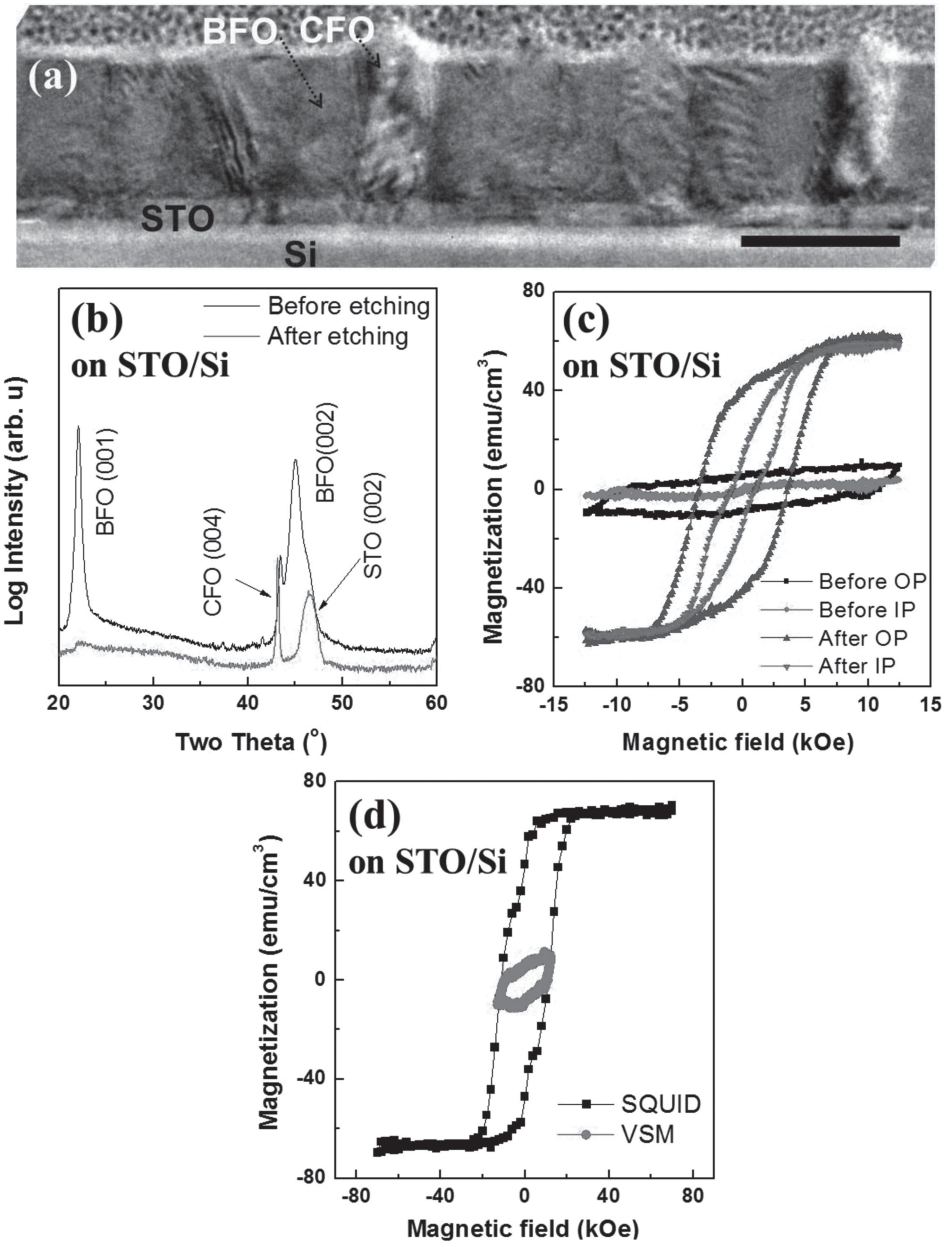

Figure 5. (a) Low magnification cross sectional TEM image of BFO-CFO nanocomposite on STO/Si. Scale bar corresponds to 50 nm. (b) XRD patterns of as deposited and etched BFO-CFO/STO/Si. (c) Magnetic hysteresis loops of BFO-CFO/STO/Si substrate before and after etching to remove BFO. (d) Out-of-plane magnetization of BFO-CFO/STO/Si substrate by SQUID and VSM at room temperature.

anisotropy. The anisotropy fields increased with the out-of-plane compression of the CFO, which was controlled by epitaxy with the BFO. Removal of the BFO matrix relaxed the strain and lowered the anisotropy. For samples grown on STF35, the STF35 provides an additional magnetic signal with out of plane anisotropy.

This work illustrates that spinel-perovskite nanocomposites can be integrated onto Si, with the 8 nm MBE-grown STO buffer layer providing a particularly thin and convenient substrate, and that the magnetic properties of the CFO pillars are highly dependent on their strain state. These results are relevant to the incorporation of epitaxial nanocomposites on a Si platform for multiferroic or magnetic memory and logic devices.

4. Experimental Section

Thin Film Growth Process: YSZ, CeO_2, $Sr(Ti_{0.65}Fe_{0.35})O_3$ (STF35) and BFO-CFO nanocomposite thin films were prepared on (001) Si (a_{Si} = 5.431 Å) by pulsed laser deposition (PLD) using a laser wavelength of 248 nm (KrF laser) and ceramic targets prepared by a conventional oxide method. Detailed deposition conditions for the growth of the BFO-CFO composite and STF on buffered Si were reported elsewhere.[18–20,22] STF35 films were prepared on CeO_2/YSZ/Si at a high vacuum of 2×10^{-6} Torr and 680 °C and were ferromagnetic with a (001) orientation.[23] The BFO-CFO nanocomposite was deposited at 5 mTorr oxygen pressure and 600 ~ 630 °C using alternating deposition from two targets, BFO and CFO. The thickness of YSZ, CeO_2, STF35 and BFO-CFO composite confirmed by cross sectional SEM images were

80, 80, 120 and 80–100 nm, respectively. For comparison, BFO-CFO was deposited on a (001) STO substrate at the same time with the same deposition conditions. Some nanocomposites were integrated on rough STF35 films grown higher temperature to investigate the relations between CFO pillar nucleation behavior and surface morphology. 8 nm epitaxial STO was deposited onto Si by MBE. A complex multistep procedure monitored in situ using reflection high energy electron diffraction is required to obtain a smooth template for subsequent growth of the nanocomposites.[12] One key step is the initial surface cleaning. Smooth starting surfaces were prepared by cleaning the surface with a strong oxidant (3:1 H_2SO_4:H_2O_2, 130 °C, 10 min), followed by removal of the native oxide (3:70 HF:H_2O, 30 s). A thin oxide (0.5 – 1 nm thick) was reformed on the surface after exposure to UV light in air for 30s. This thin oxide was then easily desorbed at 900 °C in ultrahigh vacuum, avoiding the formation of large SiO_2 mounds that often limit surface roughness, especially on the scale of the nanocomposites studied here. Desorption of the oxide was then followed by the deposition of STO using the procedure described in the literature.[12] The STO was grown at a substrate temperature of 600 °C to a total thickness of 8 nm. The surface roughness was 1 nm without surface features over 10 nm high.

Characterization of Structure and Magnetic Properties: Structure and phase formation of films were investigated by X-ray diffractometer (XRD, PANalytical X'Pert Pro) and high resolution XRD (HRXRD, Bruker-AxsD8). Strain state, epitaxial growth, and in-plane and out-of-plane lattice parameters of the buffer layer, STF35, and the nanocomposite were measured using reciprocal space mapping (RSM). Top view images of nanocomposites were taken with scanning electron microscopy (SEM, Helios Nanolab 600). The vertical spinel growth behavior was investigated using high resolution transmission electron microscopy (HRTEM, JEOL 2010F) on a sample prepared with a focused ion beam (FIB) after depositing 20 nm thickness of carbon and Pt. To confirm the 3D structure and to relax the strain of CFO some samples were etched with 10% dilute hydrochloric acid (HCl) for 60 s to remove the BFO and rinsed with DI water. The magnetic properties of films were measured by vibrating sample magnetometer (VSM, ADE model 1660) with the applied field from –10 kOe to 10 kOe and superconducting quantum interference device (SQUID) magnetometry with the applied field from –70 kOe to 70 kOe at room temperature. The linear background signal from the substrate and holder was subtracted.

Supporting Information

Supporting Information is available from the Wiley Online Library or from the author.

Acknowledgements

This work was supported by FAME, one of six STARnet centers of SRC supported by MARCO and DARPA, and by the National Science Foundation. Shared facilities of CMSE under NSF Award DMR 0819762 were used. Work at Yale was supported by the National Science Foundation under MRSEC DMR 1119826 (CRISP) and DMR-1309868.

Received: May 5, 2014
Revised: June 2, 2014
Published online: July 24, 2014

[1] H. Zheng, J. Wang, S. E. Lofland, Z. Ma, L. Mohaddes-Ardabili, T. Zhao, L. Salamanca-Riba, S. R. Shinda, S. B. Ogale, F. Bai, D. Viehland, Y. Jia, D. G. Schlom, M. Wuttig, A. Roytburd, R. Ramesh, *Science* **2004**, *303*, 661.
[2] S.-C. Liao, P.-Y. Tsai, C.-W. Liang, H.-J. Liu, J.-C. Yang, S.-J. Lin, C.-H. Lai, Y.-H. Chu, *ACS Nano* **2011**, *5*, 4118.
[3] J. Li, I. Levin, J. Slutsker, V. Provenzano, P. K. Schenck, R. Ramesh, J. Ouyang, A. L. Royburd, *Appl. Phys. Lett.* **2005**, *87*, 072909.
[4] Q. Zhan, R. Yu, S. P. Crane, H. Zhang, C. Kisielowski, R. Ramesh, *Appl. Phys. Lett.* **2006**, *89*, 172902.
[5] R. Comes, H. Liu, M. Khokhlov, R. Kasica, J. Lu, S. A. Wolf, *Nano Lett.* **2012**, *12*, 2367.
[6] M. Alexe, J. F. Scott, C. Curran, N. D. Zakharov, D. Hesse, A. Pignolet, *Appl. Phys. Lett.* **1998**, *73*, 1592.
[7] Z. Hu, M. Li, S. Pu, X. Liu, B. Sebo, X. Zhao, S. Dong, *Appl. Phys. Lett.* **2012**, *100*, 252908.
[8] M. Dekkers, M. D. Nguyen, R. Steenwelle, P. M. te Riele, D. H. A. Blank, G. Rijnders, *Appl. Phys. Lett.* **2009**, *95*, 012902.
[9] J. Kreisel, M. C. Weber, N. Dix, F. Sánchez, P. A. Thomas, J. Fontcuberta, *Adv. Funct. Mater.* **2012**, *22*, 5044.
[10] R. Bachelet, P. de Coux, B. Warot-Fonrose, V. Skumryev, J. Fontcuberta, F. Sánchez, *J. Appl. Phys.* **2011**, *110*, 086102.
[11] R. Bachelet, P. de Coux, B. Warot-Fonrose, V. Skumryev, J. Fontcuberta, F. Sánchez, *Thin Solid Films* **2011**, *519*, 5726.
[12] D. P. Kumah, J. W. Reiner, Y. Segal, A. M. Kolpak, Z. Zhang, D. Su, Y. Zhu, M. S. Sawicki, C. C. Broadbridge, C. H. Ahn, F. J. Walker, *Appl. Phys. Lett.* **2010**, *97*, 251902.
[13] J. W. Reiner, A. M. Kolpak, Y. Segal, K. F. Garrity, S. Ismail-Beigi, C. H. Ahn, F. J. Walker, *Adv. Mater.* **2010**, *22*, 2919.
[14] S. Sawamura, N. Wakiya, N. Sakamoto, K. Shinozaki, H. Suzuki, *Jpn. J. Appl. Phys.* **2008**, *47*, 7603.
[15] N. Wakiya, S. Sawamura, K. Tanemura, M. Sano, N. Sakamoto, D. Fu, K. Shinozaki, H. Suzuki, *Jpn. J. Appl. Phys.* **2009**, *48*, 09KB06.
[16] W. Zhang, A. Chen, F. Khatkhatay, C.-F. Tsai, Q. Su, L. Jiao, X. Zhang, H. Wang, *ACS Appl. Mater. Interfaces* **2013**, *5*, 3995.
[17] F. Khatkhatay, A. Chen, J. H. Lee, W. Zhang, H. Abdel-Raziq, H. Wang, *ACS Appl. Mater. Interfaces* **2013**, *5*, 12541.
[18] D. H. Kim, L. Bi, P. Jiang, G. F. Dionne, C. A. Ross, *Phys. Rev. B* **2011**, *84*, 014416.
[19] D. H. Kim, N. M. Aimon, L. Bi, G. F. Dionne, C. A. Ross, *J. Appl. Phys.* **2012**, *111*, 07A918.
[20] D. H. Kim, N. M. Aimon, L. Bi, J. M. Florez, G. F. Dionne, C. A. Ross, *J. Phys.: Condens. Matter* **2013**, *25*, 026002.
[21] H.-S. Kim, L. Bi, H. Paik, D.-J. Yang, Y. C. Park, G. F. Dionne, C. A. Ross, *Nano Lett.* **2010**, *10*, 597.
[22] D. H. Kim, N. M. Aimon, X. Sun, C. A. Ross, *Adv. Funct. Mater.* **2013**, *24*, 2334.
[23] H.-S. Kim, L. Bi, D. H. Kim, D.-J. Yang, Y. J. Choi, J. W. Lee, J. K. Kang, Y. C. Park, G. F. Dionne, C. A. Ross, *J. Mater. Chem.* **2011**, *21*, 10364.
[24] H. Zheng, Q. Zhan, F. Zavaliche, M. Sherburne, F. Straub, M. P. Cruz, L.-Q. Chen, U. Dahmen, R. Ramesh, *Nano Lett.* **2006**, *6*, 1401.
[25] H. Zheng, F. straub, Q. Zhan, P.-L. Yang, W.-K. Hsieh, F. Zavaliche, Y.-H. Chu, U. Dahmen, R. Ramesh, *Adv. Mater.* **2006**, *18*, 2747.
[26] H. Luo, H. Yang, S. A. Baily, O. Ugurlu, M. Jain, M. E. Hawley, T. M. McCleskey, A. K. Burrell, E. Bauer, L. Civale, T. G. Holesinger, Q. X. Jia, *J. Am. Chem. Soc.* **2007**, *129*, 14132.
[27] N. M. Aimon, H. K. Choi, X. Y. Sun, D. H. Kim, C. A. Ross, *Adv. Mater.* **2014**, *26*, 3063.
[28] D. H. Kim, N. M. Aimon, C. A. Ross, *J. Appl. Phys.* **2013**, *113*, 17B510.
[29] Z. Wang, R. Viswan, B. Hu, V. G. Harris, J.-F. Li, D. Viehland, *Phys. Status Solidi RRL* **2012**, *6*, 92.
[30] N. Dix, R. Muralidharan, J. Guyonnet, B. Warot-Fonrose, M. Varela, P. Paruch, F. Sánchez, J. Fontcuberta, *Appl. Phys. Lett.* **2009**, *95*, 062907.
[31] F. Zavaliche, T. Zhao, H. Zheng, F. Straub, M. P. Cruz, P.-L. Yang, D. Hao, R. Ramesh, *Nano Lett.* **2007**, *7*, 1586.
[32] N. M. Aimon, D. H. Kim, H. K. Choi, C. A. Ross, *Appl. Phys. Lett.* **2012**, *100*, 092901.